ASME Journal of Engineering for Gas Turbines and Power
Online journal at:
https://asmedigitalcollection.asme.org/gasturbinespower

Simon Vella
Department of Mechanical Engineering,
University of Bath,
Bath BA2 7AY, UK

Peter Darby
Department of Mechanical Engineering,
University of Bath,
Bath BA2 7AY, UK

Mauro Carnevale
Department of Mechanical Engineering,
University of Bath,
Bath BA2 7AY, UK

James A. Scobie
Department of Mechanical Engineering,
University of Bath,
Bath BA2 7AY, UK

Gary D. Lock
Department of Mechanical Engineering,
University of Bath,
Bath BA2 7AY, UK

Clément Jarrossay
Safran Aircraft Engines,
Villaroche, Moissy-Cramayel 77550, France

Francesco Salvatori
Safran Aircraft Engines,
Villaroche, Moissy-Cramayel 77550, France

Damien Bonneau
Safran Aircraft Engines,
Villaroche, Moissy-Cramayel 77550, France

Carl M. Sangan[1]
Department of Mechanical Engineering,
University of Bath,
Bath BA2 7AY, UK
e-mail: c.m.sangan@bath.ac.uk

A Combined Experimental and Turbulence-Resolved Modeling Approach for Aeroengine Turbine Rim Seals

Ingress is the penetration of hot mainstream gas into the rotor–stator wheel-space formed between adjacent disks; a rim seal is installed at the periphery of the wheel-space. Purge flow is bled from the compressor and re-introduced in the turbine to reduce, or in the limit prevent, ingress. This study presents a unique, concomitant experimental and turbulence-resolved numerical investigation of ingress in an aeroengine rim seal, with leakage flow. Experimental modeling is conducted in the University of Bath's 1-stage turbine test facility. Measurements of gas concentration, pressure and swirl were used to assess the performance of the rim seal. A parallel study using improved delayed detached eddy simulations (IDDES) was used to generate time-averaged and time-resolved flow-fields, enabling direct comparison with experimental data. The modeled geometry included realistic features typical of aeroengine architectures, including a contoured stator undershroud and an omega-seal cover plate. Such features were shown to locally distort the flow field, highlighting the limitation when modeling simplified geometry. The circumferential distribution of sealing effectiveness was nonaxisymmetric and synchronized in accordance with the local radial velocity field. Utilization of a detached eddy simulation (DES) turbulent kinetic energy (TKE) dissipation multiplier demonstrated regions where increased turbulence resolution was required to resolve the appropriate scale of turbulent eddies. IDDES computations were found to accurately capture the radial distributions of pressure, swirl and effectiveness, both in the absence and presence of a superposed leakage flow, provided that the mesh was sufficiently refined so as to resolve $\geq 50\%$ of the energy cascade. The IDDES approach exhibited significantly superior agreement with experiments when compared to previous studies that employed the unsteady Reynolds-averaged Navier–Stokes (URANS) methodology. [DOI: 10.1115/1.4064803]

Keywords: aeroengine turbine rim seals, improved delayed detached eddy simulation (IDDES), high fidelity computations, cavity flows

1 Introduction

There are increasing environmental concerns associated with emissions from aerospace propulsion, with associated large-scale research efforts to achieve decarbonization targets. Aeroengines are considered a mature technology, and advancement must be achieved by evolving the current fundamental understanding of rotating flows and instabilities in complex engine-representative geometries.

Secondary air systems redistribute high pressure air diverted from the compressor. This secondary flow acts as a sealing flow: it pressurizes the wheel-space between the rotor and stator, reduces ingress, and governs component life by limiting metal temperatures and thermal stresses. Using careful design, this sealing flow (or purge) enters the wheel-space at low radius (the bore) but there are also inherent leakage paths to the cavity.

A turbine rim seal is fitted to the circumferential periphery of the wheel-space cavity so as to minimize the required purge flow. There is a critical balance between superfluous use of secondary flow,

Turbomachinery Technical Conference & Exposition, Hynes Convention Center, June 26–30, 2023. Turbo Expo 2023.
[1]Corresponding author.
Manuscript received November 22, 2023; final manuscript received February 2, 2024; published online March 22, 2024. Editor: Jerzy T. Sawicki.

which reduces compressor efficiency, and insufficient use, which could lead to undesirable levels of ingress. Egress occurs for all cavity conditions as a direct result of the continuity of mass: flow ingested into the cavity must be balanced by an ejection of fluid from the cavity. Egress increases with increased sealing flow and there is an associated, complex mechanism of mixing losses with the mainstream flow in the annulus.

Typically, investigations use simplified cavity geometries characterized from mainly cylindrical surfaces. In this configuration, there is Batchelor-type flow [1] with separate boundary layers on rotating and stationary walls and an inviscid core. The flow in the boundary layer moves radially outward on the rotor and inward on the stator, with axial migration as illustrated in Fig. 1, from Tang et al. [2]. Boundary layers and a pumping effect are driven by shear, while the resultant pressure gradient is driven by swirl. The theoretically formulated system can be further described through the application of the Taylor-Proudman theorem [3], which predicts zero axial velocity gradient in rotationally dominant flows.

Engine-representative cavities feature increasingly complex geometries and compressibility effects, where simplified models such as Batchelor-type flow are not appropriate. Computational investigations such as those conducted by Horwood et al. [4] modeled a chute seal using unsteady Reynolds-averaged Navier–Stokes (URANS) methodologies, computing the formation of more complex inherently unsteady vortical instabilities, previously reported by Cao et al. [5]. These findings revealed complexities driving ingress that were not captured by classical mechanisms in simplistic geometries. The numerical results of Horwood et al. [4] were found to be in fair agreement with experiments conducted at low rotational Reynolds number ($Re_\Phi \sim 10^6$) but struggled to correctly predict ingress at high purge. The same seal geometry was experimentally investigated at KTH Royal Institute of Technology (KTH) at up to $Re_\phi \approx 4 \times 10^6$. The study performed by Roy et al. [6] on the KTH rig demonstrated a weak effect of Re_ϕ on the effectiveness and therefore ingress mechanisms.

1.1 Leakage Flows. The inevitable parasitic leakage due to pathways between the mating interfaces of engine hardware, such as chordal hinge leakage flow adds further complexity. Patinios et al. [7] experimentally assessed the impact of leakage in addition to the low radius superposed flow (purge flow). The leakage was introduced radially inboard of the vane shroud and created a toroidal vortex that extended radially inward when increasing leakage flowrate. Darby et al. [8] extended this work by conditioning the momentum and swirl of the injection into the cavity of a simple double lip rim seal. It was found that injecting leakage coswirling with the disk, improved effectiveness by up to 15%; this was associated with a reduction in the swirl gradient between the rim seal and the mainstream.

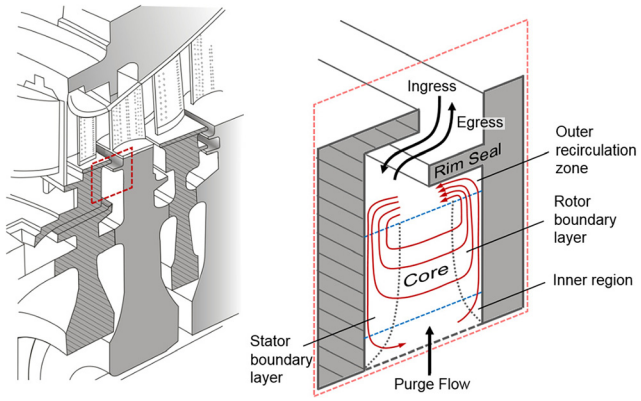

Fig. 1 Turbine stage and simplified model of rotor–stator flow structure (Tang et al. [2])

1.2 Computational Fluid Dynamics Strategy in Cavity Flows. Turbine rim seal fluid mechanics present a challenging problem, largely due to the difference in spatial and temporal scales defining two entirely different flows interacting within the rim seal region. Here, large-scale unsteady structures form and are transported circumferentially, as first identified both computationally and experimentally by Cao et al. [5]. Interactions between mainstream and cavity flows are complex and not yet fully understood. It is currently realized that such interactions are dominated by a shear contribution manifesting as a result of a viscous effect, an acoustic effect, geometry, and flow regimes. Thus, much abstractionism exists surrounding a convincing explanation of how such structures impact the sealing effectiveness. Therefore, computational fluid dynamics (CFD) is necessary to help uncover the true mechanisms driving such unsteady fluid interactions, not derivable from experiments nor through low order theoretical modeling.

Wang et al. [9] performed a 360 deg URANS simulation of a turbine rim seal geometry. They observed the formation of complex pressure patterns, not only resulting from vane and blade interactions from potential-effects but also due to turbulent mixing in the cavity. Computations of ingress using the 360 deg case have no imposed constraints due to the periodic face, which impact rim seal instability prediction. The study also indicated that purge flows were shown to form an irregular pressure pattern radially outboard of the rim seal due to vane and blade interactions. In their review of ingress, Chew et al. [10], stated that URANS modeling has a fundamental shortcoming associated with the uncertainty in turbulence modeling. The flow in turbine rim seal cavities is fundamentally unsteady and dominated by complex flow modes. Higher fidelity numerical methods with increased turbulence resolution should be considered. Large eddy simulation (LES) and direct numerical simulation (DNS) offer substantial improvements in turbulence modeling and reliability.

Pogorelov et al. [11] performed an LES simulation on a 360 deg cavity (with no wall model). Good agreement was found with experimental data and long wavelength instabilities were captured, a detail notoriously difficult to capture with one or two-equation turbulence models as required by URANS for closure. However, only simplified rim seal geometries were studied and the methodology required significant computational resources, inappropriate for widespread industrial design. A wall-modeled large eddy simulation (WMLES) methodology was presented for a chute-type rim seal by Palermo et al. [12], where computations were conducted without rotor blades. The WMLES method was introduced to reduce computational time and resource requirements compared to LES. Comparisons to experiment were quantitatively satisfactory, but an overprediction of the measured sealing effectiveness, particularly in the inner part of the cavity, was observed. The omission of the rotor blades was a limitation known to cause modulating pressure fields with a direct impact upon the swirl and pressure in the wheel-space. A more complete system featuring blades was completed by Hösgen et al. [13] utilizing a Monotone Integrated LES approach to model the subgrid contribution. Although a limited comparison was presented, improved agreement with experimental data was obtained, clearly demonstrating the requirement for turbulence resolution.

1.3 Improved Delayed Detached Eddy Simulations Theoretical Background. Element counts generally required for LES scale with $Re^{1.8}$ near wall and with $Re^{0.4}$ in the freestream are as suggested by Tucker [14]. The high demand of grid resolution required for LES and DNS makes turbulence-resolved simulation prohibitive other than for moderate Reynolds numbers. A promising strategy lies in the adoption of hybrid methods combining URANS and LES: RANS calculations are applied in the attached boundary layer region and LES methodologies in the separated flow regime. Detached eddy simulation (DES) is a hybrid RANS-LES approach. Spalart [15] provides a detailed conceptual history of DES and thoroughly describes the strengths and weaknesses of the numerical strategy. DES has been extensively applied to cavity flows over a

range of Mach numbers, consistently yielding close agreement with experiments (Allen et al. [16], Langtry et al. [17] and Mendonça et al. [18]).

The DES concept was extended by Menter et al. [19] to alleviate a Grid-Induced Separation effect. This numerical dispersion occurs when the DES limiter is falsely induced inside attached boundary layers of increasingly refined grids. A function acting to "shield" the boundary layer from the influence of the DES was therefore introduced; this is the Delayed DES (DDES) concept. Shur et al. [20] developed the improved delayed DES (IDDES) mathematical scheme to avoid the occurrence of LES incursion into the boundary layer. The approach branches the model into DDES and WMLES in the LES region of the solver, containing subgrid length-scales optimized for performance from both branches and their coupling. This provides an improved transition between LES and RANS. IDDES has significantly expanded the potential sphere of application of DDES [21].

Establishing a cogent explanation of the fundamental fluidic mechanisms driving ingress in complex engine-realistic turbine rim seals still remains an open problem. The strategy employed in this paper was to investigate the fundamental fluid dynamics in a combined experimental and numerical analysis of a scaled aeroengine rim real geometry with superposed purge and leakage flows. The modeled geometry included realistic features typical of aeroengine architectures, highlighting the limitations that arise when simulating simplified rim seal models. The novel implementation of an IDDES turbulence resolved numerical modeling technique in this context is here described. This has enabled an assessment of seal performance across a range of engine conditions using a less computationally intensive technique, in line with current industrial requirements.

2 Experimental Facility

The University of Bath's 1-stage turbine simulates ingestion from the mainstream gas path into a wheel-space formed between the adjacent disks; the rig has been configured here to model a Safran Aircraft Engines (SAE) rim seal geometry. An assembly schematic has been provided in Fig. 2. The rig operates on design at fluid dynamically scaled conditions, at an engine-representative C_F with a rotational Reynolds number 10^6 and vane exit Mach number 0.32.

The single-stage turbine consists of a stator featuring 28 vanes and a rotor blisc featuring 56 symmetric rotor blades. Due to the symmetric nature of the rotor blades, no power is generated by the stage when operating at the design condition; hence, the blisc is independently driven by a WEG Ie2 AC motor capable of generating a maximum disk speed of 4000 RPM.

The operating conditions at the design point are summarized in Table 1. Parameters are tuned to ensure a constant $C_F = 0.51$ for all experiments reported here.

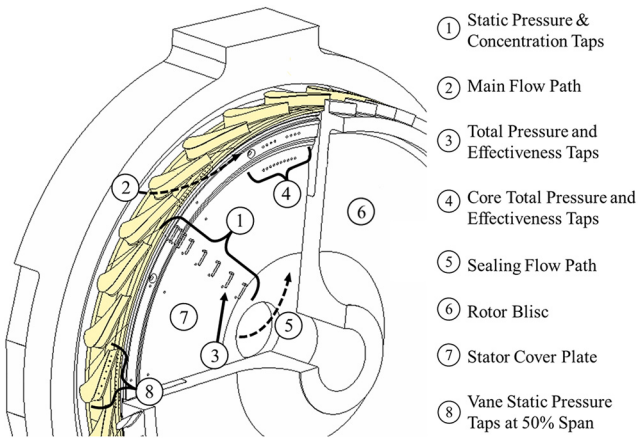

Fig. 2 Experimental turbine test stage

Table 1 Operating conditions

Parameters	
Disk speed (Ω)	3500 rpm
Rotational Reynolds number (Re_ϕ)	8.9×10^5
Axial-flow Reynolds number (Re_W)	4.60×10^5
Main flow mass-flow rate ($\dot{m}_a$)	0.54 kgs^{-1}
Flow coefficient (C_F)	0.51
Vane exit Mach number (M)	0.32
Superposed leakage ratios ($R_{\dot{m}}$)	0, 0.33, 0.5, ∞

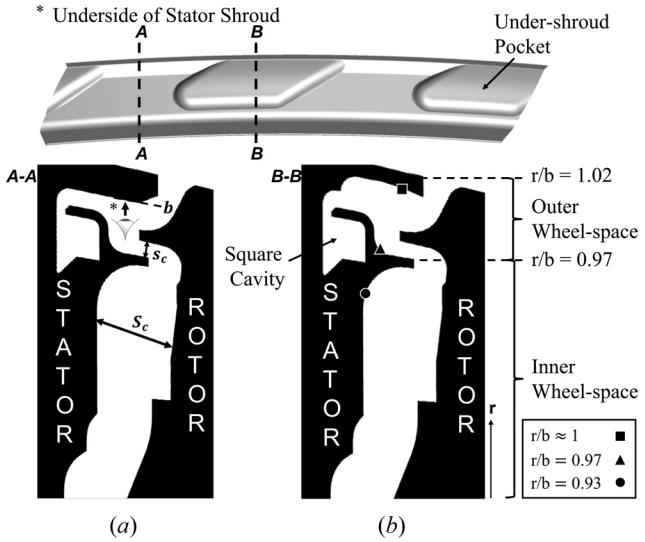

Fig. 3 Cross sections of the rim seal at (*a*) [A–A] θ/Θ=0.67, (*b*) [B–B] θ/Θ=0.18. Silhouettes are skewed to comply with confidentially agreements. The stage consists of a cylindrical annulus. The asterisk identifies the view of the underside of the stator shroud, defining the extent of the pockets.

Compressed air was supplied to the mainstream annulus through a supply line capable of providing up to 0.7 kg/s; purge flow was supplied through the bore of the stator disk via an independent flow inlet. Separate control systems comprising of Kinetrol valves coupled with a calibrated orifice plate was utilized to meter the annulus supply, and Bronkhorst thermal mass flowmeters used to measure the supply of purge and leakage flows. The mainstream flow passes through a diffuser with 28 supply pipes (one per vane), ensuring an evenly distributed flow around the annulus. The facility has been equipped with instrumentation to capture steady pressure and local species concentration throughout the stage and rim seal.

A normalized nondimensional purge flow parameter is defined as $\bar{\Phi}_B$:

$$\bar{\Phi}_B = \frac{\Phi_B}{\Phi_{B,\min *}} \tag{1}$$

where

$$\Phi_B = \frac{\dot{m}_B}{2\pi s_c \rho \Omega b^2} \tag{2}$$

$\Phi_{B,\min}$ is the minimum purge flow required to seal the wheel-space. Therefore, if $\Phi > \Phi_{\min}$, the wheel-space is sealed and ingress does not occur. $\Phi_{B,\min *}$ is the value of Φ_B where $\varepsilon_c = 1$ at $r/b = 0.93$, inside the inner wheel-space, where b is taken to be the minimum radial extent of the underside of the stator shroud (Fig. 3(*a*)).

2.1 Seal Configurations and Leakage Flow Path. Figure 3 presents the main characteristics of the rim seal geometry, including

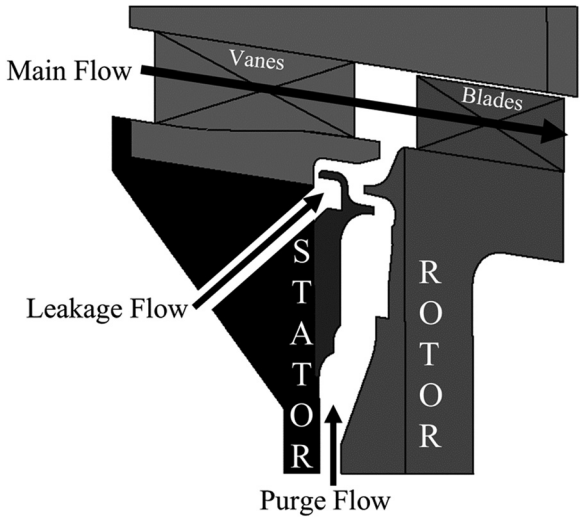

Fig. 4 Geometry of the wheel-space, identifying flow paths

manufacturing pockets and a chamfer on the leading-edge of the rotor-side platform. The double seal can be seen to divide the wheel-space into two distinct regions: an inner and outer wheel-space.

Leakage flow is fed through a manifold supplied from a secondary 2-inch line with 28 outlets (one per vane), connected to the turbine stage with flexible nylon tubing. The fluid is introduced through discrete ports and fed into a high-radius cavity located at the periphery of the stator (Fig. 4); typically an omega-type seal is fitted in this cavity to seal the chordal hinge, as modeled by the complex geometry. The cavity pressurizes when leakage flow is introduced, ensuring a circumferentially uniform flow into the outer wheel-space.

Φ_0 is defined as the *total* secondary flow supplied to the wheel-space and can be calculated by summing the nondimensional purge and leakage flows:

$$\Phi_0 = \Phi_B + \Phi_L \tag{3}$$

where Φ_B can be recalled from Eq. (2) and

$$\Phi_L = \frac{\dot{m}_L}{2\pi s_c \rho \Omega b^2} \tag{4}$$

The ratio of superposed flows is defined as, $R_{\dot{m}}$:

$$R_{\dot{m}} = \frac{\Phi_L}{\Phi_B} = \frac{\dot{m}_L}{\dot{m}_B} \tag{5}$$

A range of superposed flow ratios were tested inclusive of the extremities: $R_{\dot{m}} = 0$ (purge flow only) and $R_{\dot{m}} = \infty$ (leakage flow only). Two additional ratios were arbitrarily selected within the region of interest.

2.2 Undershroud Pockets. Additive layer manufacturing using stereolithography was used for the nozzle guide vane doublets. The design included nonaxisymmetric undershroud pockets that are commonplace in real aeroengine vane doublets. This feature improves the ease of manufacture and assembly of the engine-stage.

The geometry of the pockets and their effect on the wheel-space cross section can be seen in Fig. 3, introducing a nonaxisymmetry to the outer wheel-space, which could perturb the transport of ingested annulus gas. Two assessment locations were extracted at $\theta/\Theta = 0.18$ corresponding to midpoint of the manufacturing pocket, and $\theta/\Theta = 0.67$ midpoint between adjacent pockets. Θ is defined as the dimensionless vane pitch, starting at the trailing edge.

2.3 Instrumentation. A gas concentration technique was utilized to assess the level of ingress from the annulus into the wheel-space, whereby the purge flow was seeded with a tracer gas: ~1% CO_2. Hence, the sealing effectiveness (ε_c) is defined as:

$$\varepsilon_c = \frac{c - c_a}{c_0 - c_a} \tag{6}$$

where c is the local CO_2 concentration, normalized by values measured in the annulus (subscript a) and in the purge flow prior to injection into the wheel-space (subscript 0). c_a takes account of the inherent CO_2 concentration in air ($c_a \approx 0.04\%$).

CO_2 concentration was measured using a Signal Group 9000 MGA multigas analyzer connected to a 20-channel multiplexor. Fifteen sampling ports were distributed on the stator wall, as depicted in Fig. 2. The gas analyzer had an associated accuracy, repeatability, and linearity of $\pm 0.5\%$ on its full-scale range, which was 1% CO_2 throughout this study.

The 15 sampling ports were also used to assess the radial distribution of static pressure. A Scanivalve was used to connect the ports to a single differential pressure transducer, with a measurement uncertainty of $\pm 0.06\%$ (Best Straight Line) of the full-scale range over a range of 70 mbar.

Pitot probes were fitted 2.7 mm proud of the stator disk to assess the radial distribution of total pressure, aligned to the tangential direction. Due to the wheel-space geometry, the wheel-space width (S_c, defined in Fig. 3) changes radially, which results in the nondimensional Pitot tube positions relative to S_c varying between $0.41 \leq r/S_c \leq 0.63$. Local swirl ratio is defined as follows:

$$\beta = \frac{V_{\theta\infty}}{\Omega r} \tag{7}$$

where the tangential component of velocity in the core, V_{θ_∞}, was calculated through Bernoulli's principle using static and total pressure measurements.

3 Computational Fluid Dynamics Modeling Approach

Hybrid RANS/LES simulations were carried out in conjunction with the experimental campaign; the IDDES approach employed the commercial package, ANSYS FLUENT. The implementation consists of a modified RANS solver employing SST k-ω for turbulence closure. The model has been equipped with an algorithm permitting the numerical method to switch to a subgrid scale formulation in regions where discretization is fine enough for LES calculations. IDDES embedded in ANSYS is based on the $k-\omega$ model as detailed in Gritskevich et al. [22]. WMLES were employed for the regions where turbulence scales were resolved.

The CFD domain periodicity was reduced to a 26 deg sector model with two vanes, four blades and featuring two leakage inlet ports—illustrated in Fig. 5. A sliding plane interface between stationary and rotating domains was defined upstream of the rim seal leading edge. Fluidic boundary conditions were applied to the model representative of the turbine design point (Table 1). The computational setup consisted of mass flow boundary conditions at the main and sealant inlets. A turbulent intensity of 5% and turbulent viscosity ratio equal to 10 was applied across both inlet conditions. A radial equilibrium pressure distribution was also employed at the outlet. The passive scalar was introduced through a low-radius inlet (representative of the experimental setup) to enable the quantification of rim seal ingestion.

The computational mesh consisted of $\sim 14 \times 10^6$ elements. Computational methodologies derived from Spalart's original DES formulation [23] maintain a constant grid resolution independent of turbulence scheme. This provides a significant advantage in terms of computational resource compared to zonal Hybrid URANS-LES methodologies, such as that proposed by Almendral-Fernandez et al. [24]. Here, domain zones require independent utilization of RANS or LES on distinct mesh files, coupled with a computationally expensive exchange algorithm. Convergence of the passive scalar was reached after $\sim 12 - 20$ rotor revolutions, depending upon the

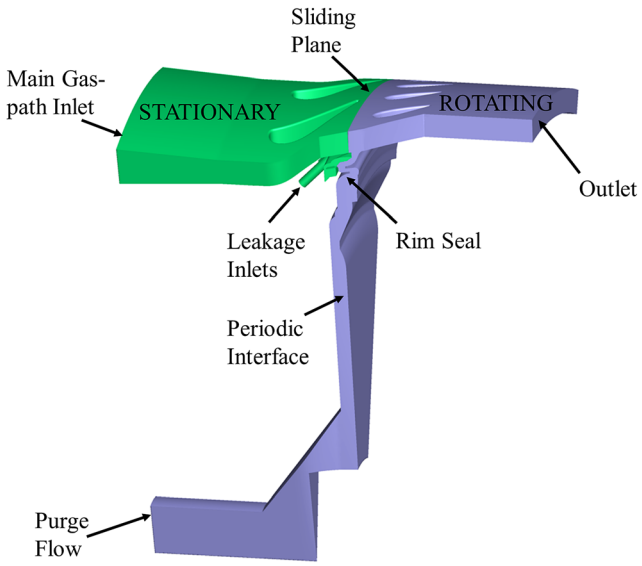

Fig. 5 CFD domain and boundary conditions, with explicit definition of the stationary (green) and rotating frames (purple), for the case of superposed leakage flow. (Color version online.)

superposed purge mass flowrate. Computations were typically completed utilizing 500 cores, requiring approximately 9 core hours per revolution.

3.1 Assessment of Large Eddy Simulation Mesh Resolution.

The use of an unstructured polyhedrally tessellated grid is necessary to reduce the mesh skewness typically occurring when discretizing complex geometries. A coupled pressure–velocity scheme of the Rhie-Chow distance based flux type in an extended cell stencil was implemented, evaluating gradients through a least squares cell-based approach. Field variables were assessed utilizing a second-order upwind method. The boundary layers were discretized with prismatic elements.

An increased level of turbulence anisotropy was captured and modeled as a result of the grid resolution. Appropriate levels of mesh refinement were applied at the vane trailing edge and throughout the rim seal, in order to capture the flow instabilities pertinent to the ingress phenomenon. The mesh refinement close to the wall ensured an average $y^+ = 0.380$ on the rotor-side and $y^+ = 0.227$ on the stator-side. The following mesh refinement statistics were determined in the freestream of the rim-seal region: $\Delta x^+ = 8.228$, $\Delta\theta^+ = 8.975$ and $\Delta r^+ = 8.493$.

Jefferson-Loveday [25] concluded that extensive a priori grid assessment should be conducted for each specific configuration when working with hybrid RANS-LES models. To ensure turbulent content is being resolved here, extreme caution was taken to guarantee that adequate turbulence resolution and sufficient LES application was present throughout the rotor–stator domain.

In this study, mesh resolution has been set based on the definition of the integral length-scale l_0. It represents an average of all of the turbulent scales at a local point in a region of the flow and can be approximately estimated from a precursory RANS simulation (as required to initiate a turbulence resolved computation) based on the Kolmogorov energy spectrum as $l_0 = k^{1.5}/\varepsilon = k^{0.5}/(C_\mu \omega)$, where $C_\mu = 0.09$. Using the resolution of the smallest resolved length-scale, l, which requires at least two cells in each direction, a metric $\Delta \approx \frac{l}{2} \approx \sqrt[3]{(V_{\text{Cell}})}$ can be defined to approximate the LES mesh resolution. Evaluating the relationship of the cumulative TKE against the eddy integral length-scale as derived from Kolmogorov's energy spectrum, the following criteria can be derived to evaluate the extent of TKE resolution:

- $k(l) = 0.5k \rightarrow [l_0/\Delta = 1.25]$
- $k(l) = 0.8k \rightarrow [l_0/\Delta = 4.80]$

The instantaneous l_0/Δ has been evaluated at the $\theta/\Theta = 0.18$ and $\theta/\Theta = 0.67$ localities to quantify the TKE resolution, with particular attention to the rim seal and outer wheel-space locations. This was necessary due to the asymmetry of the undershroud geometry. Figure 6 illustrates radial contours at the two assessment locations between the 50% and 80% cumulative TKE equivalencies for the $\bar{\Phi}_B = 0.67 (\Phi_L = 0)$ purge flow only case. At this particular time-step, the TKE resolution seen upon entrance to the outer wheel-space and at the rim seal exit where egress plumes are exhausted into the mainstream annulus are $\geq 80\%$, thus corresponding to very significant turbulence resolution.

The resolved-to-modeled turbulent length scale ratio has been identified by the blending parameter $\chi \geq 1$, defined as the DES TKE

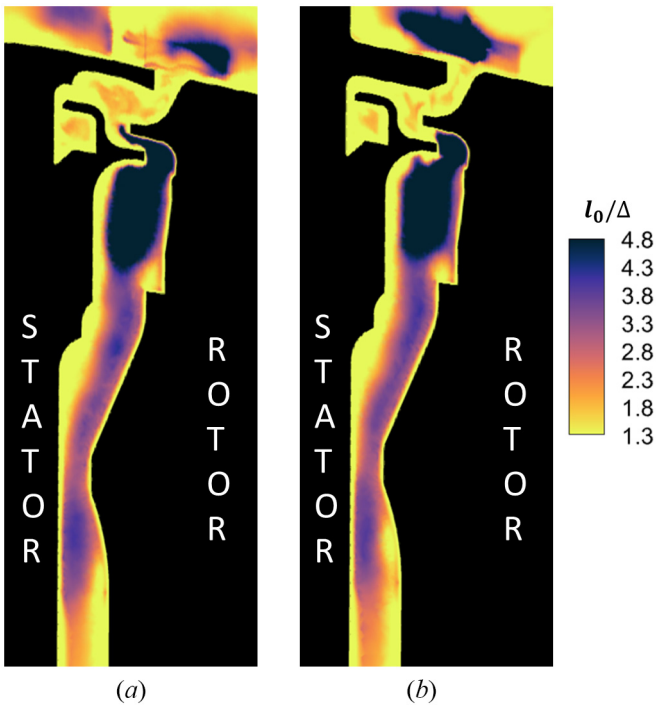

Fig. 6 Assessment of mesh resolution in LES using instantaneous turbulent kinetic energy resolution criterion for the $\bar{\Phi}_B$=0.67 case: (*a*) θ/Θ=0.18 and (*b*) θ/Θ=0.67

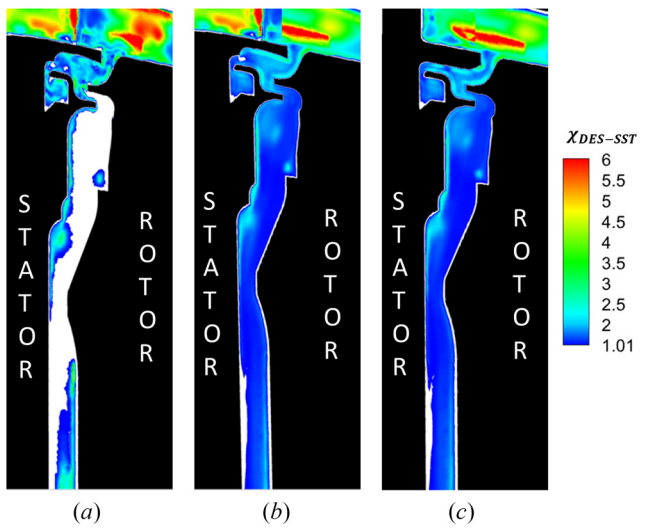

Fig. 7 DES TKE dissipation multiplier: (*a*) instantaneous (χ) θ/Θ=0.18, (*b*) time-averaged ($\bar{\chi}$) θ/Θ=0.18, and (*c*) time-averaged ($\bar{\chi}$) θ/Θ=0.67. The contour is clipped at 1.01 so only the LES solution is shown; RANS is employed where $\chi \leq 1$.

dissipation multiplier. χ is employed to identify the ratio between the modeled and resolved turbulence scales. Pure RANS regions are identified where $\chi = 1$. For increasing χ, the resolved part of the turbulence scales become predominant and asymptotically tends to LES. Figure 7(*a*) illustrates the instantaneous radial distribution of χ, whilst 7(b) and (c) highlight the time-resolved, therefore $\bar{\chi}$ (relative to the case $\bar{\Phi}_B = 0.67[\Phi_L = 0]$), where white areas highlight regions solved with RANS and therefore no LES was applied. Similarly to Fig. 6, cross sections were extracted at two angular positions ($\theta/\Theta = 0.18$ and $\theta/\Theta = 0.67$), throughout the extent of the rim seal and outer wheel-space.

The instantaneous distribution of χ shown in Fig. 7(*a*) identified two distinct regions with different turbulent length-scales. This is in agreement with the work of Horwood et al. [4], who claim that RANS is not sufficient to predict the shear-driven eddies evolving within the rim seal. However, this is not necessarily the case in the wheel-space, where the turbulent length-scale is larger and therefore more appropriate to be computed through a turbulence model rather than being directly resolved. Therefore, when considering the implementation of a hybrid RANS-LES technique, LES resolution is reserved for the rim seal and mainstream gas path.

3.2 Postprocessing Algorithm. To enable comparison with experimental probe locations (Fig. 2), scalar values of interest must be extracted both within and at the boundaries of the domain. This is a challenge when profiles are extracted along polylines as the solver is cell-centered and the domain is discretized by polyhedrons. Therefore, a postprocessing algorithm has been developed based on the KD-Tree binary nearest neighbors search algorithm in a *k*-dimensional space, popular in computer science applications such as that described by Zhang et al. [26] to solve the Fokker-Planck equation. Data points are organized through a space-partitioning data structure at each leaf node, creating splitting regions; thus, the nearest neighbors search can be substantially accelerated. The essential element in building a KD-Tree is to compare inserted points through all considered dimensions; hence, as the scheme progresses, all axes are cycled through to identify splitting regions required for an individual query point, as shown in Fig. 8(*a*).

The computational solution is assessed as a point cloud and the derived algorithm is used to find the vertices in the full volume that are closest to defined target vertices (e.g., corresponding to a desired angular location on the stator wall consistent with the measurement location of the test facility). Field variables corresponding to filtered volume vertices are therefore also identified. Filtered discrete volume vertices in Euclidean space can then be triangulated using Delaunay triangulation and an interpolated field can be calculated through a barycentric weighted average interpolation, mapping the scalar field (Fig. 8(*a*)).

The true novelty in the employment of such an in-house postprocessing algorithm is the opportunity to specify any multi-dimensional target path or volume. Thus, the developed algorithm is well-suited to the analysis of field variables at the wall of complex cavities (Fig. 8(*b*)) and other such applications within turbomachinery.

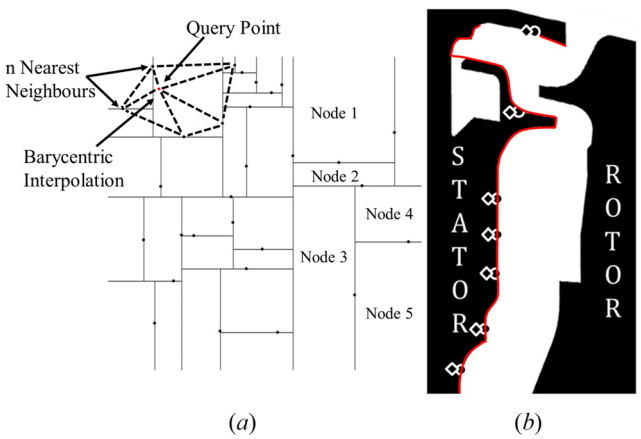

Fig. 8 (*a*) A branched and binary search 2D KD-Tree approach through the creation of a series of leaf nodes. (*b*) Illustration of CFD extraction surfaces. The solid line defines the geometry, while the dashed line outlines the undershroud pocket, neglected as $r/b>1$. Experimental measurement locations are shown in diamonds and circles.

4 Results

In this section, time-averaged IDDES computations of pressure, swirl, and effectiveness are compared with measurements obtained from the University of Bath's single-stage axial turbine experimental facility acquired in the presence and absence of leakage flows. Computational results for pressure and effectiveness are extracted along the stator-side surface as outlined in Fig 8(*b*), where the shroud region has been neglected (i.e., $r/b > 1$). Swirl values have been extracted 2.7 mm off the stator-side surface, consistent with experimental measurements. The validity of IDDES results is scrutinized in the context of an engine-realistic turbine rim seal configuration. Finally, more complex fluidic mechanisms relating to rotor-side radial inflow are discussed in detail.

4.1 Analysis of Purge Flow Only Cases. The validation of the IDDES numerical model is presented from an aerodynamic

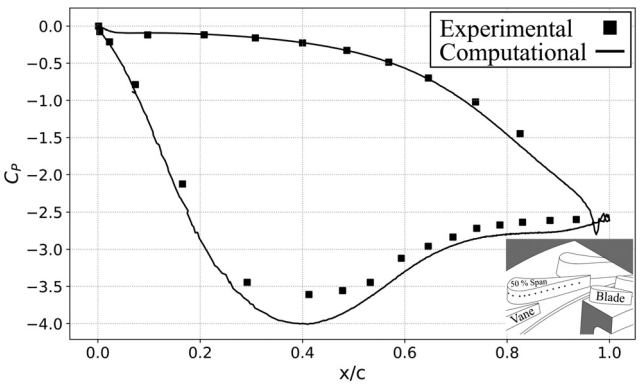

Fig. 9 Aerodynamic vane loading at 50% span for $\bar{\Phi}_B$=0.67

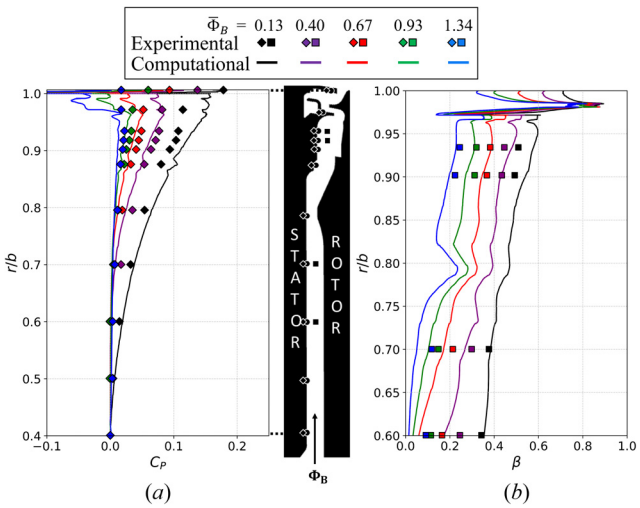

Fig. 10 Radial distribution of (*a*) time-averaged pressure coefficient and (*b*) swirl in the rim seal and wheel-space over a range of purge flow levels. Note that the swirl data are not aligned to the silhouette.

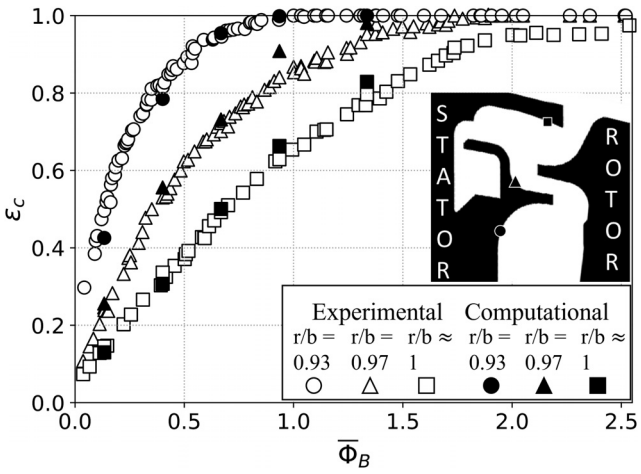

Fig. 11 ε_c variation with $\bar{\Phi}_B$ at r/b=0.93, r/b=0.97 and $r/b \approx 1$. Experiments are open symbols; computations are solid symbols.

perspective. Figure 9 presents vane loading at 50% span for $\bar{\Phi}_B = 0.67$. Experiments and simulations conducted over a range of purge flows exhibited a consistent vane loading due to the relatively large distance between the vane trailing-edge and turbine rim seal. The IDDES computation overestimates the vane loading at the midchord. The absence of a significant fish-tail at the vane trailing-edge indicates appropriate mesh quality in this region [27].

Further validation of the CFD computations was achieved through comparison with stator-side pressure and swirl measurements as shown in Fig. 10. Measurement locations extend from the lower wheel-space to the underside of the stator shroud; data are acquired for pressure up to $r/b \approx 1$ and swirl up to $r/b = 0.93$. A silhouette of the wheel-space is lined up with the ordinate of Fig. 10(*a*). Good qualitative agreement between experimental and computational datasets can be seen for both fluid dynamic quantities. A constant underestimation of C_P magnitude exists for $\bar{\Phi}_B > 0.13$; a broad overprediction is present for $\bar{\Phi}_B = 0.13$.

The radially increasing static pressure on the stator wall (Fig. 10(*a*)) is indicative of core circulation. A reversal in pressure gradient ($\partial p/\partial r$) occurs at $r/b \approx 0.97$, before it is substantially increased to a corresponding maximum β at $r/b \approx 0.98$. This is associated with the presence of three distinct zones: the inner and outer wheel-spaces, as well as an intermediate transition region between them. Bru Revert et al. [28] reported similar inflexions in pressure gradient and related the reduction in swirl as the flow passes into the outer wheel-space to an increased surface area per unit radial distance. The effect can be attributed to relative stator-side drag [29], retarding the swirl in this region. This mechanism has been captured by the IDDES computations, demonstrating that such a viscous effect exists in the inner seal clearance, reducing the local tangential component of velocity accordingly.

Flow in the outer wheel-space reaches a maximum rotational speed of $\sim 90\%$ of the disk speed for $\bar{\Phi}_B = 0.13$ (as $\beta \to 1$ in the region $0.97 \leq r/b \leq 0.98$). The local decrease in swirl at $r/b > 0.98$ is driven by the gradient in swirl that exists between the annulus and the wheel-space. This was discussed in detail by Graikos et al. [30] who demonstrate that ingress has a significant dependence upon the swirl in the annulus.

Figure 11 presents the experimental and numerically predicted distribution of effectiveness with purge flow. Effectiveness has been measured at three different radial locations: $r/b = 0.93$, $r/b = 0.97$ and $r/b \approx 1$. Conforming with classical rotor–stator disk cavity theory, the superposition of increased purge mass flow results in the sealing of the wheel-space, first in the inner and then the outer wheel-space. The outermost measurement location ($r/b \approx 1$) does not attain complete sealing, exhibiting turbulent diffusion for $\bar{\Phi}_B \geq 2.0$, whereby mass is transferred between the cavity and annulus due to the dispersion associated with mixing. Computational predictions exhibit good agreement with experimental measurements for the $r/b = 0.93$ and $r/b \approx 1$ locations. However, considering the measurement location at $r/b = 0.97$, an overprediction in effectiveness is seen for values of $\bar{\Phi}_B > 0.67$. This discrepancy is associated with less accurate prediction of C_P in regions where a strong radial gradient of pressure exists (Fig. 10(*a*)).

The IDDES agreement outlined in Fig. 11 presents a significant improvement over URANS computations, such as that of Horwood

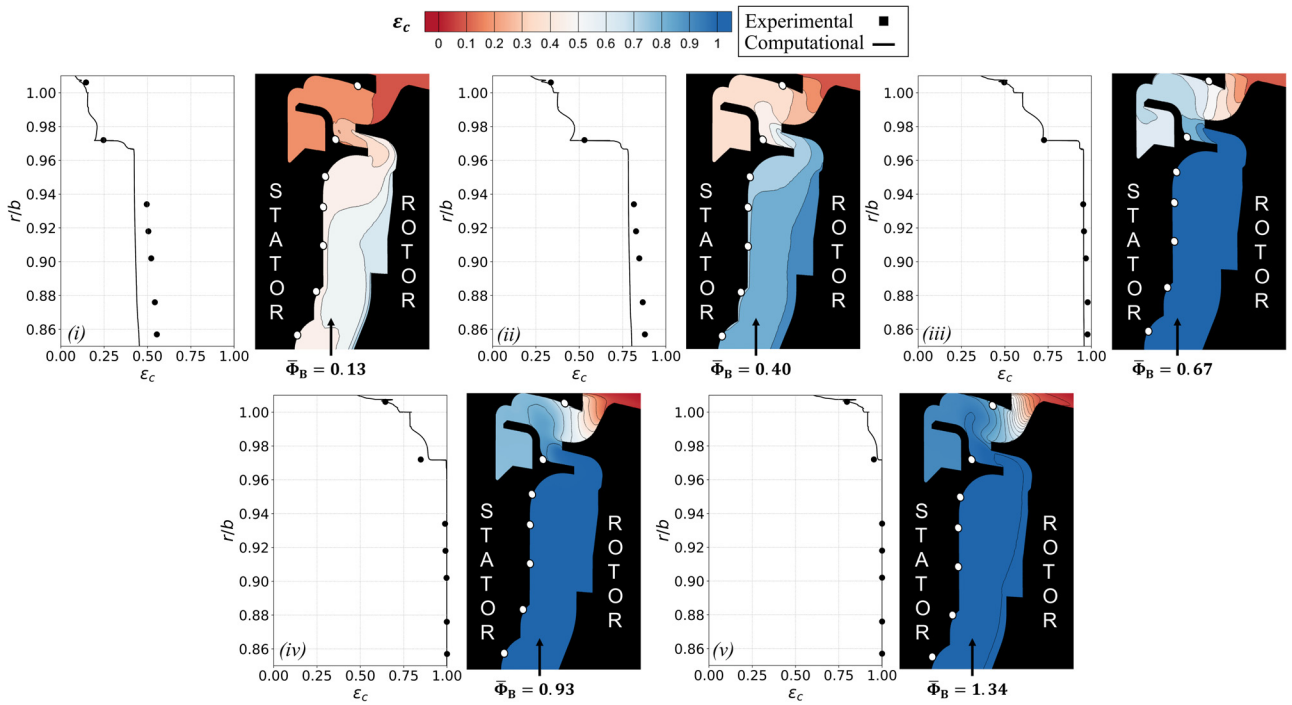

Fig. 12 Radial distribution of time-averaged effectiveness at θ/Θ=0.18 (i) $\bar{\Phi}_B$=0.13, (ii) $\bar{\Phi}_B$=0.40, (iii) $\bar{\Phi}_B$=0.67, (iv) $\bar{\Phi}_B$=0.93, and (v) $\bar{\Phi}_B$=1.34. Contours of effectiveness from IDDES are superimposed on silhouettes of the wheel-space, aligned to the ordinates.

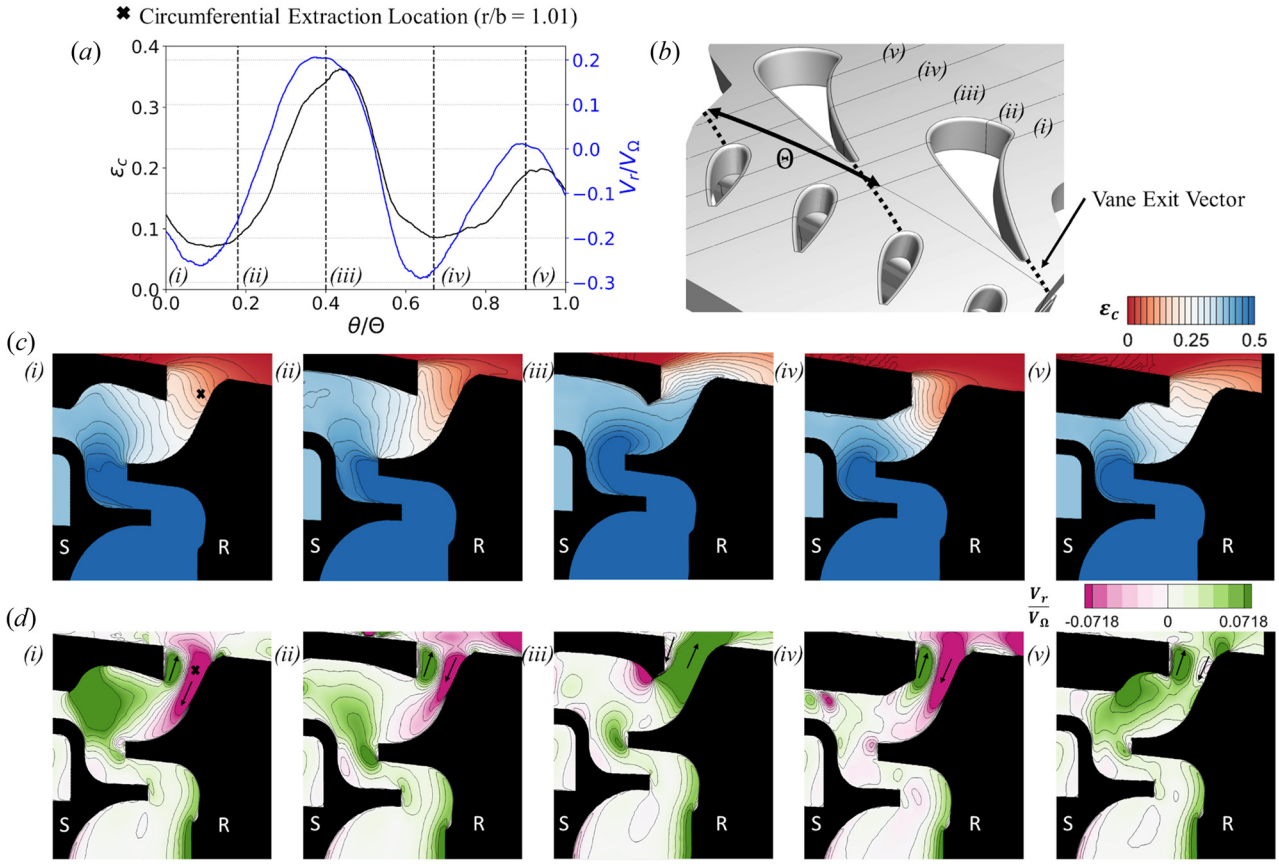

Fig. 13 (*a*) Circumferential variation of time-averaged ε_c and V_r/V_Ω across a vane pitch. (*b*) Extraction planes across a vane pitch. Contours of (*c*) time-averaged ε_c, and (*d*) V_r/V_Ω for $\bar{\Phi}_B$=0.40. (i) θ/Θ=0, (ii) θ/Θ=0.18, (iii) θ/Θ=0.40, (iv) θ/Θ=0.67, (v) θ/Θ=0.90. Here, *S* indicates the stator-side and *R* the rotor-side. V_r has been nondimensionalized with respect to the linear disk velocity at r/b=1.

et al. [31] who obtained a root-mean-square error equal to 0.172 in the rim seal at $r/b = 0.96$ when comparing to experimental data across a range of Φ_B. The IDDES computations reported here reduce this discrepancy by an order of magnitude, achieving a substantially reduced relative error of 0.034 at the $r/b = 0.93$ location, 0.032 at $r/b = 0.97$ and 0.022 at $r/b \approx 1$ while considering a greater sample size.

In fact, radial distributions of time-averaged effectiveness shown in Fig. 12 for five purge flow rates demonstrate qualitative agreement in the order of the LES computations of Hösgen et al. [13] and Pogorelov et al. [11], vastly surpassing that which can be attained through a URANS-only computation. Contour plots are superimposed on silhouettes aligned to the ordinates. An increase in purge flowrate corresponds to an increase in effectiveness. The mixing region (corresponding to bunched isocontours of effectiveness) is progressively displaced radially outward with purge. Savov et al. [32] describe a similar assessment for a double lip geometry.

The gradient in effectiveness, $\partial\varepsilon_c/\partial r$, seen in Fig. 12 between $0.97 \leq r/b \leq 1$ can be interpreted as an assessment of the relative local mixing between ingested flow in the outer wheel-space and flow exiting the inner wheel-space. Considering initially the cases of $\bar{\Phi}_B = 0.13$ and $\bar{\Phi}_B = 1.34$, (i) and (v) in Fig. 12, $\partial\varepsilon_c/\partial r$ is reduced in comparison to intermediate purge flow levels as the mixing is predominantly confined to the inner and outer seal clearances, respectively.

The radial distribution of effectiveness highlights the overprediction of ingress in the inner wheel-space at lower purge flows ((i) and (ii)), while conversely underpredicting ingress in the outer wheel-space for (iii), (iv), and (v) at high purge flow rates. Here, the accurate prediction in effectiveness is consistent with the prediction of β in the inner wheel-space when $\bar{\Phi}_B \leq 0.67$.

Contours in Fig. 12 clearly demonstrate a thermal buffering effect, particularly apparent at lower purge flows. A high effectiveness region forms on the rotor-side of the inner wheel-space due to the disk pumping effect. The purge flow serves to protect the rotor disk from ingested high temperature flow from the annulus; lower values of effectiveness are exhibited at consistent radii on the stator-surface.

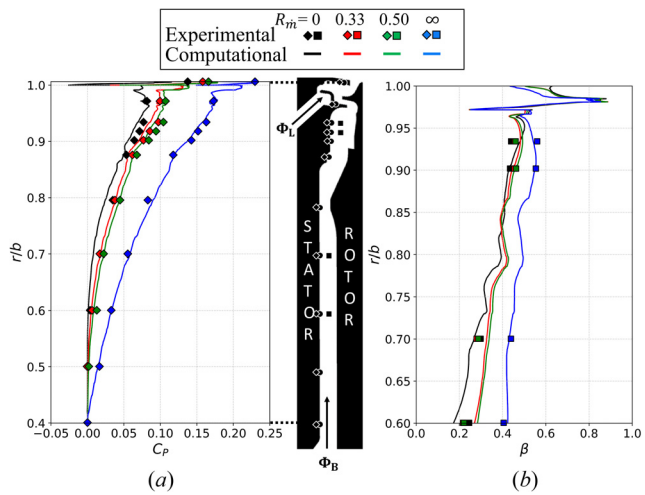

Fig. 14 Radial distribution of (*a*) time-averaged pressure coefficient and (*b*) swirl for three levels of leakage flow at a constant $\bar{\Phi}_B$=0.40. Note that the swirl is not aligned to the silhouette.

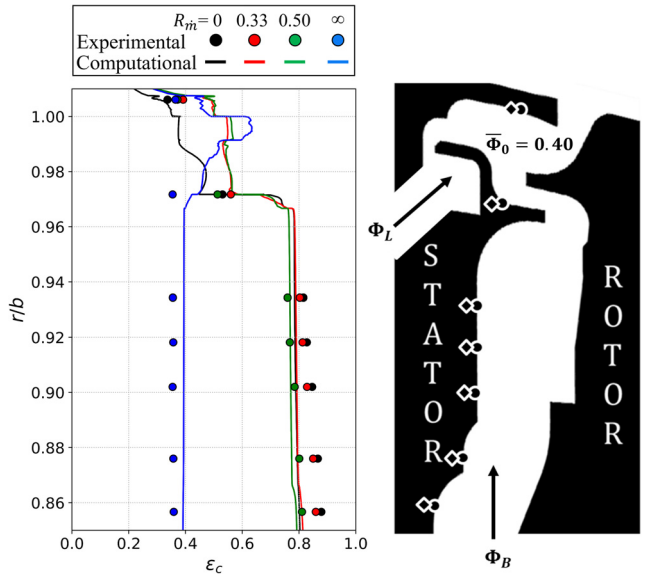

Fig. 15 Radial distribution of time-averaged effectiveness for three levels of leakage flow at a constant $\bar{\Phi}_0$=0.40

Fundamentally, the transport of ingested mainstream fluid can be interpreted as a scalar predominantly governed by two processes: diffusion and convection. Analysis of the radial component of velocity, which is independent of the frame of reference, describes the convective contribution to the transport of the passive scalar, which is indicative of ingress. Figure 13 provides the circumferential variation of the time-averaged values for effectiveness and radial velocity across a vane pitch at the $\bar{\Phi}_B$ condition. Five cross sections are extracted at different θ in order to allow for the nonaxisymmetry introduced by the presence of the pocket to be captured. Analysis of time-averaged field variables in the absolute frame of reference removes any effect related to the clocking position of the rotor.

Circumferential distributions of V_r/V_Ω and ε_c have been extracted near the rotor hub at $r/b = 1.01$, as shown in Figs. 13(*a*) and 13(*b*). Both quantities exhibit a synchronous sinusoidal distribution with θ. Contours of effectiveness and radial velocity are extracted at five pitchwise planes, identified in Fig. 13(*b*) and presented as Figs. 13(*c*) and 13(*d*), respectively. Considering planes (i), (ii), and (iv), a local decrease in ε_c is seen adjacent to the rotor wall, corresponding to the convective effect driven by locally negative radial velocity V_r/V_Ω. This effect has been defined by De Cosmo et al. [33] as a shallow ingress mechanism. V_r/V_Ω describes the convective transport effect of the ingested fluid. However, ε_c is a function of both convective and diffusive transport effects, the visible phase lag ($\theta/\Theta \approx 0.08$) between field variables is indicative of the latter. This phase lag amplifies when in alignment with the minimum radial seal clearance (plane iv), demonstrating the impact of the contoured geometry upon concentration gradient.

The contours in Fig. 13(*c*) at planes (i) and (ii) align with the absolute frame vane exit swirl vector, considering its projection in the relative frame of reference. The impact of the vane exit swirl effect can be seen to enhance rotor-side ingress into the rim seal. However, the presence of the ingress peak at plane (iv) suggests that the vane effect is not the sole driver for ingestion. Instead, the nonaxisymmetry of the stator-side undershroud creates a local nonuniformity in the flow field, impacting the transport of ingested annulus fluid. Velocity profiles predicting a rotor-side radial inflow have been previously identified by Horwood et al. [4] while modeling a chute rim seal using URANS. Gao et al. [34] predicted an even more pronounced rotor-side inflow with LES. Location (iv) does exhibit radial inflow on the rotor-side, and does not align to the vane effect argument. Instead, this plane corresponds to a

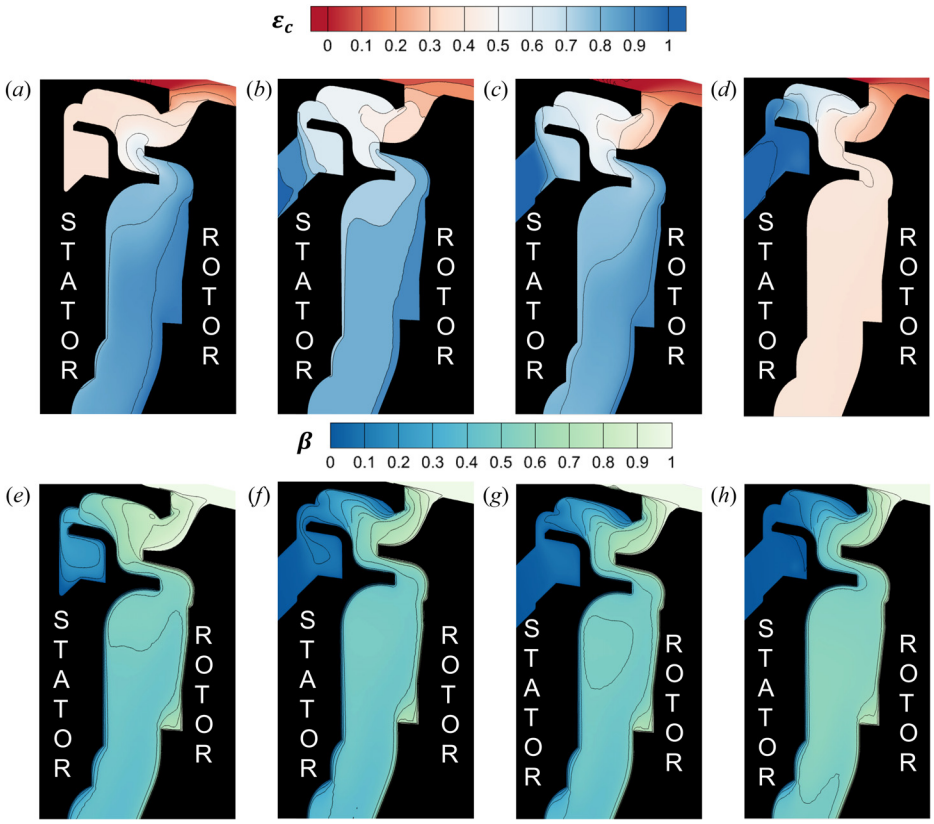

Fig. 16 Contours of (*a*) time-averaged effectiveness and (*b*) time-averaged swirl at θ/Θ=0.40: (i) R_m=0, (ii) R_m=0.33, (iii) R_m=0.5, and (iv) R_m=∞

circumferential location between the manufacturing pockets and it is hypothesized that the local fluid mechanics are altered by a significant reduction in mixing volume.

4.2 Superposition of Leakage Flow. Time-averaged radial distributions of pressure, swirl, and effectiveness are presented here for the case of superposed leakage flow. To the authors' knowledge, this work presents the first high-fidelity turbulence resolved computations of high-radius leakage flow in the literature; comparisons are made with experiments specifically designed to validate the computations. All tests reported here were conducted at a constant $\bar{\Phi}_0 = 0.40$, inclusive of the $R_{\dot{m}} = \infty$ case, where all flow is introduced from the leakage ports.

Figure 14 presents radial distributions of static pressure and swirl, exhibiting good quantitative and qualitative agreement between experiment and computation for all tested $R_{\dot{m}}$. Swirl is shown to be almost independent of the ratio of superposed flows when $\Phi_B > \Phi_L$. The computations accurately predict the local decrease in pressure as fluid radially exits the inner wheel-space, while also exhibiting a subsequent increase in pressure toward the shroud due to the addition of the superposed leakage flow.

A comparison of experiments and computations of high-radius leakage flow on the radial distribution of effectiveness is outlined in Fig. 15. Generally, IDDES computations exhibit reasonable agreement with experimental measurements for all radial positions.

It is evident that ingress is sensitive to the introduction of a high-radius leakage flow. However, assuming that $\Phi_B > \Phi_L$, the magnitude of $R_{\dot{m}}$ is less influential upon rim seal performance in the inner wheel-space. Experimental datasets converge upon a value of $\varepsilon_c \approx 0.38$ at $r/b \approx 1$, indicating that ingestion is insensitive to Φ_L at the periphery of the wheel-space. Therefore, the total superposed fluid (i.e., purge, leakage and ingested annulus fluid) can be considered as fully mixed. For radial locations in the outer wheel-space ($r/b \geq 0.97$), computations predict a local increase in effectiveness with $R_{\dot{m}}$ for all leakage cases (compared to a baseline case with solely purge flow), and therefore reduced ingestion of annulus gas. The inner wheel-space, however, exhibits an opposing trend, whereby increased annulus gas is permitted to penetrate deeper into the cavity—an effect, which is exacerbated as $R_{\dot{m}}$ is increased and therefore the introduced purge mass flow is reduced.

Contours of swirl and effectiveness are presented in Fig. 16, extracted at the midplane of a leakage inlet ($\theta/\Theta = 0.40$). The addition of high-momentum leakage flow progressively displaces the mixing region in the outer wheel-space radially outward through the rim seal and into the main gas path. A strong axial gradient of swirl can be seen from stator to rotor, which intensifies as $R_{\dot{m}}$ increases—illustrated by the bunching of swirl isocontours. The axial gradient of swirl seen in Fig. 16 suppresses the vortex-dominated flow structure proposed in Patinios et al. [7], an effect not present when considering simplified rim seal geometries.

The circumferentially averaged axial distributions of time-averaged swirl and effectiveness are described at $r/b \approx 1$ (for the outer wheel-space) in Fig. 17, for the case of no leakage flow and $R_{\dot{m}} = 0.5$. The presence of leakage flow can be seen to introduce a high pressure, low swirl region in the vicinity of the stator wall. This acts to prohibit the axially inward penetration of the ingress plume, typified by the substantially increased ε_c.

$x/X = 0.64$ (outlined in Fig. 17) represents the extrema of the rim seal axial overlap. At this location, $\partial\varepsilon_c/\partial x$ increases for both leakage flow conditions; a larger extent for the case of $R_{\dot{m}} = 0.5$. The difference in ε_c between the two $R_{\dot{m}}$ cases diminishes toward the rotor-side. This suggests that for axial locations $x/X > 0.64$, the flow field experiences an increased influence from the annulus.

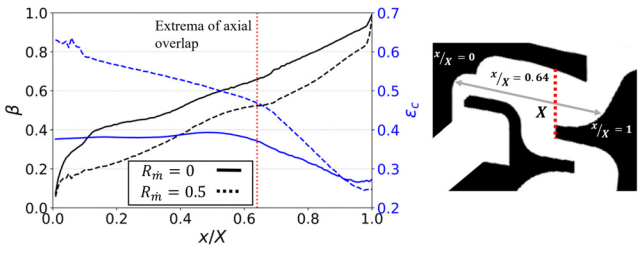

Fig. 17 Comparison of time-averaged, circumferentially-averaged axial distributions of swirl and effectiveness at $r/b \approx 1$, for the case of $R_{\dot{m}}$=0 (solid) and $R_{\dot{m}}$=0.5 (dashed). x/X=0 corresponds to the stator wall, while x/X=1 is at the rotor wall.

5 Conclusions

A concomitant experimental and computational methodology has been used to assess the performance of an aeroengine rim seal with purge and leakage flows. A complex geometry was modeled, including features prevalent in real aeroengine architectures, but seldom considered in research. Features such as a nonaxisymmetric undershroud and stator-side omega-seal cover plate were found to locally perturb the flow field and influence ingestion. This paper reports the first use of IDDES in such flows, found to present superior agreement to experimental data when compared to previous studies utilizing URANS methodologies.

Key conclusions from the study are as follows:

(1) A representative aeroengine turbine rim seal has been characterized over an extensive range of superposed purge mass flow rates. The complex rim seal conformed to classical rotor-stator disk cavity theory whereby the outer wheel-space was dominated by the ingestion of flow from the annulus and subsequent mixing, with radial inflow predominantly on the rotor-side. Turbulent diffusion—and subsequently an incomplete sealing of the outer rim seal—was observed for $\bar{\Phi}_B \geq 2.0$ due to sustained mixing between annulus and cavity flows.

(2) Computations demonstrated the suitability of IDDES for modeling ingress, provided that the mesh was sufficiently refined so as to ensure the resolution of $\geq 50\%$ of the turbulence length-scales. The DES TKE multiplier (χ) demonstrated regions in which increased turbulence resolution was required to resolve the appropriate scale of turbulent eddies. This identified the periphery of the rim seal as the focus for high fidelity calculations, whereas the inner cavity could be modeled sufficiently with a RANS approach.

(3) The vane exit swirl was shown to primarily govern the radial inflow, with a causal link identified between the bulk convection and the transport of ingested fluid (signified by the local effectiveness). However, a secondary inflow mechanism was found to be strongly related to local nonuniformity introduced by the non-axisymmetric stator-side undershroud. A phase lag of $\theta/\Theta \approx 0.08$ existed between the circumferential distribution of effectiveness and radial velocity; the lag was amplified when aligned with the radial minima of the rim seal clearance.

(4) Sealing performance was strongly impacted by the presence of a high-radius leakage flow. Experimental measurements implied a fully-mixed flow for all $R_{\dot{m}}$ and uniform effectiveness equal to ≈ 0.38. Computations indicated the presence of an axial gradient of swirl that intensified with $R_{\dot{m}}$ and progressively displaced the mixing region out of the seal clearance.

Acknowledgment

The authors would like to acknowledge the technical expertise and support of Andrew Langley for his insight throughout this project enabling the design, construction, and continued running of the experimental facility. The authors would also like to thank Safran Aircraft Engines for funding this work in its entirety. The University of Bath Library Research Strategy Open Access Fund is acknowledged for enabling this research to be open access.

Data Access

Due to confidentiality agreements with research collaborators, supporting data can only be made available to bona fide researchers subject to a nondisclosure agreement. Details of how to request access are available at the University of Bath data archive.

Data Availability Statement

The datasets generated and supporting the findings of this article are obtainable from the corresponding author upon reasonable request.

Nomenclature

Roman Letters

b = radius of seal (m)
c = concentration of tracer gas (%)
C_F = flow coefficient ($= W/\Omega b$)
C_P = pressure coefficient ($= \frac{p-p_{\text{tot}}}{\frac{1}{2}\rho\Omega^2 b^2}$)
C_μ = turbulence model constant
k = turbulent kinetic energy (J/kg)
l_0 = turbulent integral length scale (m)
M = Mach number
$\dot{m}_a$ = annulus mass flow rate (kg/s)
$\dot{m}_B$ = purge mass flow rate (kg/s)
$\dot{m}_L$ = leakage mass flow rate (kg/s)
p= static pressure (Pa)
p_{tot}= total pressure (Pa)
r = radius (m)
$R_{\dot{m}}$ = ratio of superposed flows ($= \Phi_L/\Phi_B$)
Re_W = axial-flow Reynolds number
Re_ϕ = rotational Reynolds number
s_c = rim gap clearance (m)
S_c = local seal clearance (m)
V_{Cell} = cell volume (m^3)
V_r = radial velocity component (m/s)
V_θ = tangential velocity component (m/s)
V_Ω = linearized blisc speed velocity (Ωr) at $r/b = 1$ (m/s)
y^+ = non-dimensional first mesh cell height

Greek Symbols

β = swirl ratio ($= V_{\theta\infty}/\Omega r$)
Δ = cell size (m)
ε = specific rate of dissipation of turbulent kinetic energy for $k-\varepsilon$ model (m^2/s^3)
ε_c = effectiveness derived from concentration ($= [c-c_a]/[c_0-c_a]$)
θ = local circumferential position (deg)
Θ = full extent of vane pitch (deg)
ρ = density (kg/m^3)
Φ_B = non-dimensional purge flow sealing parameter ($= \dot{m}_B/2\pi s_c\rho\Omega b^2$)
$\bar{\Phi}_B$ = normalized non-dimensional purge flow sealing parameter $\bar{\Phi}_B = \Phi_B/\Phi_{B,\min*}$
$\Phi_{B,\min*}$ = the value of Φ_B that seals the wheel-space at a non-dimensional radius of $r/b = 0.93$
Φ_L = non-dimensional leakage flow sealing parameter ($= \dot{m}_L/2\pi s_c\rho\Omega b^2$)
Φ_0 = non-dimensional total secondary flow sealing parameter ($= \dot{m}_{B+L}/2\pi s_c\rho\Omega b^2$)
χ = DES turbulent kinetic energy dissipation multiplier
ω = specific rate of dissipation of turbulent kinetic energy for $k-\omega$ model (m^2/s^3)
Ω = angular speed of rotating disk (rad/s)

References

[1] Owen, J. M. and Rogers, R. H., 1989, "Flow and Heat Transfer in Rotating-Disc Systems, Rotor-Stator Systems," Vol. 1, Research Studies Press Ltd, Taunton, UK.
[2] Tang, H., Cho, G., Patinios, M., Scobie, J. A., Sangan, C. M., Owen, J. M., and Lock, G. D., 2019, "Effect of Ingress on Flow and Heat Transfer Upstream and Downstream of a Rotating Turbine Disc," Aerospace, **6**(5), p. 49.
[3] Childs, P. R. N., 2010, *Rotating Flow*, Elsevier, Amsterdam, The Netherlands; Boston, MA.
[4] Horwood, J. T., Hualca, F. P., Wilson, M., Scobie, J. A., Sangan, C. M., Lock, G. D., Dahlqvist, J., and Fridh, J., 2020, "Flow Instabilities in Gas Turbine Chute Seals," ASME J. Eng. Gas Turbines Power, **142**(2), p. 021019.
[5] Cao, C., Chew, J., Millington, P., and Hogg, S., 2004, "Interaction of Rim Seal and Annulus Flows in an Axial Flow Turbine," ASME J. Eng. Gas Turbines Power, **126**(4), pp. 786–793.
[6] Roy, A. S., Fridh, J., Scobie, J., Sangan, C., and Lock, G., 2021, "Flow Instability Effects Related to Purge Through a Gas Turbine Chute Seal," J. Global Power Propul. Soc., **5**, pp. 111–125.
[7] Patinios, M., Ong, I. L., Scobie, J. A., Lock, G. D., and Sangan, C. M., 2019, "Influence of Leakage Flows on Hot Gas Ingress," ASME J. Eng. Gas Turbines Power, **141**(2), p. 021010.
[8] Darby, P., Mesny, A., De Cosmo, G., Carnevale, M., Lock, G., Scobie, J., and Sangan, C., 2021, "Conditioning of Leakage Flows in Gas Turbine Rotor–Stator Cavities," ASME J. Eng. Gas Turbines Power, **143**(2), p. 021009.
[9] Wang, C.-Z., Mathiyalagan, S. P., Johnson, B. V., Glahn, J. A., and Cloud, D. F., 2014, "Rim Seal Ingestion in a Turbine Stage From 360-Degree Time Dependent Numerical Simulations," ASME J. Turbomach., **136**(3), p. 031007.
[10] Chew, J. W., Gao, F., and Palermo, D. M., 2019, "Flow Mechanisms in Axial Turbine Rim Sealing," Proc. Inst. Mech. Eng., Part C, **233**(23–24), pp. 7637–7657.
[11] Pogorelov, A., Meinke, M., and Schröder, W., 2019, "Large-Eddy Simulation of the Unsteady Full 3D Rim Seal Flow in a One-Stage Axial-Flow Turbine," Flow, Turbul. Combust., **102**(1), pp. 189–220.
[12] Palermo, D. M., Gao, F., Amirante, D., Chew, J. W., Bru Revert, A., and Beard, P. F., 2021, "Wall-Modeled Large Eddy Simulations of Axial Turbine Rim Sealing," ASME J. Eng. Gas Turbines Power, **143**(6), p. 061025.
[13] Hösgen, T., Meinke, M., and Schröder, W., 2020, "Large-Eddy Simulations of Rim Seal Flow in a One-Stage Axial Turbine," J. Global Power Propul. Soc., **4**, pp. 309–321.
[14] Tucker, P. G., 2016, *Advanced Computational Fluid and Aerodynamics* (Cambridge Aerospace Series), Cambridge University Press, Cambridge, UK.
[15] Spalart, P. R., 2009, "Detached-Eddy Simulation," Annu. Rev. Fluid Mech., **41**(1), pp. 181–202.
[16] Allen, R., Mendonça, F., and Kirkham, D., 2005, "RANS and DES Turbulence Model Predictions of Noise on the M219 Cavity at M = 0.85," Int. J. Aeroacoust., **4**(1–2), pp. 135–151.
[17] Langtry, R., and Spalart, P., 2009, "Detached Eddy Simulation of a Nose Landing-Gear Cavity," IUTAM Symposium on Unsteady Separated Flows and Their Control, M. Braza and K. Hourigan, eds., Springer, Dordrecht, The Netherlands, Vol. 14, pp. 357–366.
[18] Mendonça, F., Allen, R., Charentenay, J., and Kirkham, D., 2003, "CFD Prediction of Narrowband and Broadband Cavity Acoustics at M = 0.85," AIAA Paper No. 2003-3303.
[19] Menter, F. R., Kuntz, M., and Langtry, R., 2003, "Ten Years of Industrial Experience With the SST Turbulence Model," Proceedings of the Fourth International Symposium on Turbulence, Heat and Mass Transfer, Begell House, Antalya, Turkey, pp. 625–632.
[20] Shur, M., Spalart, P., Strelets, M., and Travin, A., 2008, "A Hybrid RANS-LES Approach With delayed-DES and Wall-Modelled LES Capabilities," Int. J. Heat Fluid Flow, **29**(6), pp. 1638–1649.
[21] Wang, G., Wang, S., Li, H., Fu, X., and Liu, W., 2021, "Comparative Assessment of SAS, IDDES and Hybrid Filtering RANS/LES Models Based on Second-Moment Closure," Adv. Mech. Eng., **13**(6), p. 168781402110284.
[22] Gritskevich, M., Garbaruk, A., Schütze, J., and Menter, F., 2012, "Development of DDES and IDDES Formulations for the k-ω Shear Stress Transport Model," Flow, Turbul. Combust., **88**(3), pp. 431–449.
[23] Spalart, P., Jou, W.-H., Strelets, M., and Allmaras, S., 1997, "Comments on the Feasibility of LES for Wings, and on a Hybrid RANS/LES Approach," Conference: Advances in DNS/LES, Ruston, LA, Aug. 4–8, pp. 137–148.
[24] Almendral-Fernandez, G., Amirante, D., and Hills, N. J., 2018, "Use of a Zonal Hybrid URANS-LES Methodology for Prediction of Rim Seal Ingestion Into a Low Pressure Turbine Cavity," AIAA Paper No. 2018–4917.
[25] Jefferson-Loveday, R. J., 2019, "Enhanced Delayed Detached Eddy Simulation for Cavities and Labyrinth Seals," ASME J. Eng. Gas Turbines Power, **142**(1), p. 011017.
[26] Zhang, H., Xu, Y., Liu, Q., Wang, X., and Li, Y., 2022, "Solving Fokker-Planck Equations Using Deep KD-Tree With a Small Amount of Data," Nonlinear Dyn., **108**(4), pp. 4029–4043.
[27] Denton, J. D., 2010, "Some Limitations of Turbomachinery CFD," ASME Paper No. GT2010-22540.
[28] Bru Revert, A., Beard, P., Chew, J., and Bottenheim, S., 2021, "Performance of a Turbine Rim Seal Subject to Rotationally-Driven and Pressure-Driven Ingestion," ASME J. Eng. Gas Turbines Power, **143**(8), p. 081025.
[29] Revert, A. B., Beard, P. F., Chew, J. W., and Bottenheim, S., 2021, "Sealing Performance of a Turbine Rim Chute Seal Under Rotationally-Induced Ingestion," J. Phys.: Conf. Ser., **1909**(1), p. 012035.
[30] Graikos, D., Tang, H., Sangan, C. M., Lock, G. D., and Scobie, J. A., 2022, "A New Interpretation of Hot Gas Ingress Through Turbine Rim Seals Influenced by Mainstream Annulus Swirl," ASME J. Eng. Gas Turbines Power, **144**(11), p. 111005.

[31] Horwood, J. T. M., Hualca, F. P., Scobie, J. A., Wilson, M., Sangan, C. M., and Lock, G. D., 2018, "Experimental and Computational Investigation of Flow Instabilities in Turbine Rim Seals," ASME J. Eng. Gas Turbines Power, **141**(1), p. 011028.
[32] Savov, S. S., Atkins, N. R., and Uchida, S., 2017, "A Comparison of Single and Double Lip Rim Seal Geometries," ASME J. Eng. Gas Turbines Power, **139**(11), p. 112601.
[33] De Cosmo, G., Scobie, J. A., Lock, G. D., Sangan, C. M., and Carnevale, M., 2022, "Fluid Dynamics of Turbine Rim Seal Structures: A Physical Interpretation Using URANS," ASME J. Eng. Gas Turbines Power, **145**(3), p. 031009.
[34] Gao, F., Chew, J. W., Beard, P. F., Amirante, D., and Hills, N. J., 2018, "Large-Eddy Simulation of Unsteady Turbine Rim Sealing Flows," Int. J. Heat Fluid Flow, **70**, pp. 160–170.